

# End-to-End Pixel-Based Deep Active Inference for Body Perception and Action

Cansu Sancaktar<sup>1</sup>

Pablo Lanillos<sup>2</sup>

## Abstract

We present a pixel-based deep Active Inference algorithm (PixelAI) inspired in human body perception and successfully validated in robot body perception and action as a use case. Our algorithm combines the free energy principle from neuroscience, rooted in variational inference, with deep convolutional decoders to scale the algorithm to directly deal with images input and provide online adaptive inference. The approach enables the robot to perform 1) dynamical body estimation of arm using only raw monocular camera images and 2) autonomous reaching to “imagined” arm poses in the visual space. We statistically analyzed the algorithm performance in a simulated and a real Nao robot. Results show how the same algorithm deals with both perception and action, modelled as an inference optimization problem.

## Index Terms

Active inference, Deep learning, Free energy optimization, Bio-inspired Perception, Predictive coding, Robots.

## I. INTRODUCTION

Learning and adaptation are two core characteristics that allow humans to perform flexible whole-body dynamic estimation and robust actions in the presence of uncertainties [1]. We hypothesize that the human brain learns the representation (models) of the body since the pregnancy thanks to neural binding [2]. However, those models learnt are “flexible” making body perception highly adaptive. Experiments have demonstrated that our perception and action of the body can be altered in less than one minute just by synchronous visuo-tactile stimulation [3], [4]. This supports that unsupervised learning mechanisms within perception are being enhanced with online supervised adaptation [5]. On the contrary, robots usually use a fixed-rigid body model where the arm end-effector is defined as a pose, i.e., a 3D point in the space and an orientation. Any error in the model or change in the conditions will drive into failure.

Several solutions have been proposed to overcome this problem usually separated in perception and control approaches. For instance, by working in the visual space (e.g. visual servoing [6]) we can exploit a set of invariant visual keypoints to provide control that incorporate real world errors. Bayesian sensory fusion in combination with model-based fitting allows adaptation to sensory noise and model errors [7] and model-based active inference to provide online adaptation in both action and perception [8]. Finally, learning approaches have shown that can overcome the difference between the model and the reality, by optimizing the body parameters or by explicitly learning the policy for a task (e.g., imitation learning, reinforcement learning). Recently, model-free approaches, specially deep-RL, have demonstrated the power for directly using raw images as an input for learning visual control policies [9].

### A. Contribution

In this work, we present *PixelAI*, a pixel-based deep active inference algorithm (Fig. 1) that combines all these characteristics: works in the visual space, provides adaptation and has model-free learning; and moreover, it unifies perception and action into a single variational inference formulation. We motivated and validated the proposed approach on body perception and action. However, the algorithm can be generalized to other active perception tasks. Our algorithm allowed the robot to perform: i) dynamical body estimation using monocular raw images and ii) pixel-direct visual servoing with imaginary goals.

Technically, we combined the free energy bound optimization, which enables adaptation, with deep convolutional decoders, to learn the generative models. Our algorithm has following advantages over other methods in the literature. First of all, it is neuroscience-inspired, specifically on the predictive coding and the free-energy principle of the brain [10], [11]. This means that we can directly make comparisons with human body perception. Secondly, instead of being a black box where the features learnt are bound to the task, it is grounded to the robot body and therefore it has a physical meaning and it can be used for more complex tasks. It does not need reward engineering and works directly in the sensory space, and despite its simple implementation with a decoder, it handles both perception and action. Finally, it allows flexible/adaptive perception and it can be combined with model-based approaches.

<sup>1</sup> Institute for Cognitive Systems, Technical University of Munich, Germany. cansu.sancaktar@tum.de

<sup>2</sup> Donders Institute for Brain, Cognition and Behaviour, the Netherlands p.lanillos@donders.ru.nl

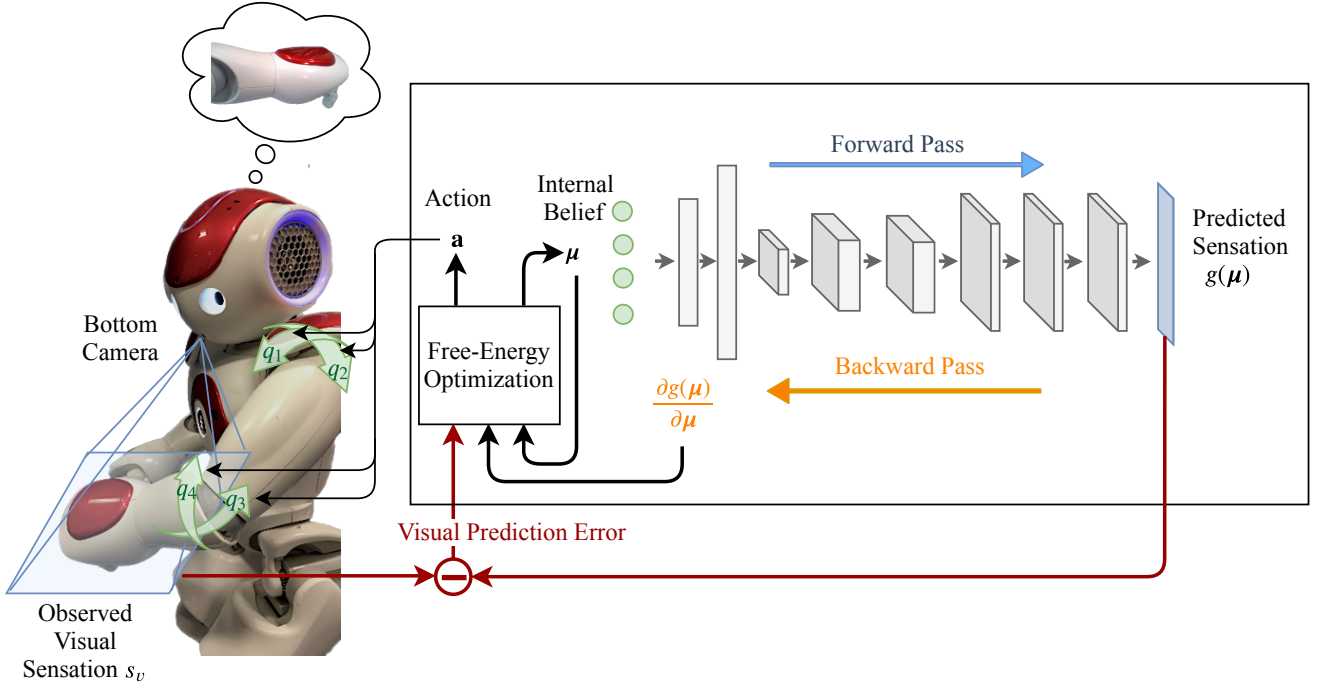


Fig. 1. Pixel-based Deep Active Inference (*PixelAI*). In the body perception and action use case, the robot infers its body (e.g., joint angles) by minimizing the visual prediction error, i.e. discrepancy between the camera sensor value  $s_v$  and the expected sensation  $g(\mu)$  computed using a convolutional decoder. The error signal is used to update the internal belief to match the observed sensation (perceptual inference) and to generate an action  $a$  to reduce the discrepancy between the observed and predicted sensations. Both are computed by optimizing the free energy bound.

### B. Neuroscience-inspired perception and action

Our approach is first grounded on human embodied research: *first the body then the policy* [12]. The robot must first learn to perceive its body (the cross-modal sensorimotor relations [13], [14]) and afterwards it should use this information to adapt to online changes when interacting and learning in the world.

We explicitly modeled our algorithm inspired by the predictive coding mathematical abstraction of the brain [10], [11]. The brain would learn the generative models of the body to aid in the reconstruction of the reality from the incoming partial multimodal information. The brain, organized in hierarchical layers, instead of directly encoding the sensory information, would process the error between the predicted outcome and the current input. In this sense, we hypothesize that body perception and action is a consequence of surprise minimization through the prediction errors. Following this approach, the robot should learn the visual latent representation (state) of the body and the relation between its state and the expected sensations (predictions). These predictions will be compared with the observed sensory data generating an error signal that can be propagated to refine the belief that the robot has about its body state. Compensatory actions would follow a similar principle and will be exerted to better correspond to the prediction made by the models learnt, giving the robot the capacity to actively adjust to online changes in the body and the environment.

### C. Goals in the sensory space

Imaginary goals in the sensory space is an easy way to encode intentions directly comparable with the observed data. When working in the visual space we provide an image as a goal. For instance, in [15] they used this approach for comparing several Deep-RL methods for the reaching task. In our case, setting the goal as the body in the visual space has a clear meaning, which is the visual representation of an arm pose.

### D. Work organization

Section II details the proposed PixelAI approach. Section III describes the experimental setup in simulation and with the real robot, as well as the training procedures. Finally, Sec. IV shows the results for robotic body perception and action.

## II. PIXEL-BASED DEEP ACTIVE INFERENCE

### A. Fundamentals

The core idea behind free-energy optimization in body perception is to infer the body state  $x$  based on the available sensory data  $s$ . Given a sensation  $s$ , the goal is to find  $x$  such that the posterior  $p(x|s)$  is maximized. Using Bayes Rule, the following is obtained:

$$p(x|s) = \frac{p(s|x)p(x)}{p(s)} \quad (1)$$

However, the computation of the marginal likelihood  $p(s)$  requires an integration over all possible body states:  $\int_x p(s|x)p(x)dx$ , which becomes intractable for large state spaces. The free-energy [16], largely exploited in machine learning and computational neuroscience [17], circumvents this problem by introducing a reference distribution  $q(x)$ . Using Jensen's inequality, the following is obtained:

$$\ln \int_x q(x) \frac{p(s,x)}{q(x)} dx \leq \int_x q(x) \ln \frac{p(s,x)}{q(x)} dx \quad (2)$$

The free-energy term to be optimized then becomes:

$$F = \int_x q(x) \ln \frac{q(x)}{p(s,x)} dx = \underbrace{\int_x q(x) \ln \frac{q(x)}{p(x|s)} dx}_{KL(q(x)\|p(x|s))} - \ln p(s) \quad (3)$$

Due to the non-negative properties of the Kullback-Leibler divergence, the variational free-energy becomes an upper bound on surprise, i.e. the negative log-evidence  $-\ln p(s)$ .

The goal of the minimization problem hence becomes finding the reference distribution  $q(x)$  that best approximates the posterior  $p(x|s)$ . However, further assumptions regarding the form of the reference distribution are needed to make this optimization problem tractable. Under the Laplace approximation, the reference distribution can be assumed to take the form of a Gaussian with  $x \sim \mathcal{N}(\mu, \Sigma)$ . The variational free-energy introduced in equation 3 can also be unpacked as:

$$F = - \int_x q(x) \ln p(s,x) dx + \int q(x) \ln q(x) dx, \quad (4)$$

By substituting the reference distribution in the equation above with a Gaussian distribution, the free-energy can be approximated as

$$F \approx L(\mu, s) - (\ln |\Sigma| + n \ln 2\pi), \quad (5)$$

where  $n$  is the dimension of the state vector  $x$ . The term  $L(\mu, s)$  is defined as the Laplace-encoded energy and is a mathematical construct for  $-\ln p(s, x)$ .

The free energy can be minimized in two ways:

- 1) Perceptual inference: The agent updates its internal belief in a way that maximizes the likelihood of the observed sensation by minimizing the free energy.
- 2) Active Inference: The agent generates an action through minimizing the free energy which in turn results in a new sensory state that is consistent with the current internal representation. Thus the prediction error is minimized.

When minimizing the free energy using a gradient descent approach, both the internal belief  $\mu$  and the action  $a$  do not depend on the second term and the optimization problem is reduced to minimizing the Laplace-encoded energy  $L(\mu, s)$ .

### B. PixelAI Algorithm

The proposed approach depicted in Fig. 1 is summarized in Algorithm 1. The agent has learnt approximate generative forward models of the world, implemented here as convolutional decoders. While interacting, the expected sensation (produced by the decoder) is compared with the real visual input and the prediction error is used to update the belief and to generate actions with the same objective: minimize the surprise. In order to update the differential equation that drives perception we exploit the error backpropagation algorithm (backward pass of the decoder) to compute the change needed in the “state” (decoder input) to minimize the free energy bound. When there is an imaginary goal in the visual space, this will work as a perceptual attractor that changes the internal belief. The derived prediction error will push the action towards the goal. In essence, *perception drives the action*.

In the use case of body perception and action,  $s_v$  is set to the image provided by the robot monocular camera and the decoder input becomes the robot proprioception (e.g. joint angles). The convolutional decoder is trained with this mapping describing the visual forward model. The prediction error  $e_v$  is the difference between the expected visual sensation and the observation (line 8). The free energy optimization for perception (line 9) and action (line 10) update the differential equations that drive the state estimation and control enabling adaptation. Finally, we added in the dynamics term the possibility of inputting imaginary goals in the visual space (line 13). Although, this implementation assumes that  $\mu' = 0$ , it is straight forward to add the 1st order dynamics when there is velocity image information or joint encoders [8].

---

**Algorithm 1** Deep Active Inference Algorithm: PixelAI

---

**Require:**  $\Sigma_v, \Sigma_\mu, \beta, \Delta_t$ 

```

1:  $\mu \leftarrow$  Initial joints angle estimation
2:  $\mu', v, \mathcal{L} \leftarrow \mathbf{0}$ 
3: while (true) do
4:    $s_v \leftarrow \text{Resize}(\text{camera image})$                                  $\triangleright$  Visual Sensation
5:    $\mathbf{g}(\mu) \leftarrow \text{ConvDecoder.forward}(\mu)$                           $\triangleright$  Predictor Sec. II-D
6:    $D_g \leftarrow \text{ConvDecoder.backward}(\mu)$                                  $\triangleright$  Sec. II-E1
7:    $\dot{\mu} \leftarrow \mathbf{0}$                                                   $\triangleright$  Active Inference
8:    $e_v = (s_v - \mathbf{g}(\mu))$ 
9:    $\dot{\mu} = \dot{\mu} + K_{vis} D_g^T e_v / \Sigma_v$ 
10:   $\dot{a} = \dot{a} - (D_g^T e_v / \Sigma_v) \Delta_t$ 
11:  if  $\exists s_{attr}$  then                                               $\triangleright$  Goal attractor  $\rho$  dynamics
12:     $e_f = -f(\mu, \rho)$ 
13:     $\dot{\mu} = \dot{\mu} - D_g^T (\beta e_f / \Sigma_\mu)$ 
14:   $\mu = \mu + \Delta_t \dot{\mu}$                                                $\triangleright$  1st order Euler integration
15:   $a = a + \Delta_t \dot{a}$ 
16:   $\text{SetVelocityController}(a)$ 

```

---

### C. Pixel-Based Free Energy Formulation

In this section, formalize the free energy principle body perception and action [8] to work directly with images.

In this problem setting, the internal body state  $\mu$  corresponds to the estimations of the robot arm joint angles, such as the shoulder pitch and roll or the elbow yaw and roll. Therefore, the robot internal belief is an  $n$ -dimensional vector ( $\mu \in \mathbb{R}^n$ ).

For our PixelAI approach, the free-energy optimization is performed solely using the visual sensory information obtained through the robot's camera. The visual sensation  $s_v$  denotes an image of size  $w \times h$ , with width  $w$  and height  $h$ .

The model also includes the causal variables  $\rho$  which encode the attractor image  $s_{attr}$ . This is equivalent to an "imagined" pose of the arm in the visual space. These causal variables are used as part of the attractor dynamics.

Using these definitions, the key term  $\ln p(s, x)$  for the Laplace encoded energy, becomes:

$$\ln p(s, \rho, \mu) = \ln p(s_v | \mu) p(\mu' | \mu, \rho) \quad (6)$$

In order to derive the form of the Gaussian analogously for the visual sensation  $s_v$ , a mapping between the internal belief of the body state and the expected visual sensation needs to be defined. This corresponds to the internal visual forward model of the robot, where for a given internal belief value  $\mu$ , the predicted camera image is computed. This non-linear function is denoted as  $\mathbf{g}(\mu) \in \mathbb{R}^{h \times w}$ .

Now that the internal computation of the visual forward model has been defined, let's assume that the observed camera image  $s_v$  is noisy and follows a normal distribution with a mean at the value of  $\mathbf{g}(\mu)$  and with variance  $\Sigma_{s_v}$ . The distribution  $p(s_v | \mu)$  is then obtained as:

$$p(s_v | \mu) = C_v \prod_{k=1}^h \prod_{l=1}^w \exp \left[ -\frac{1}{2\Sigma_{s_v}} (v_{k,l} - g_{k,l}(\mu))^2 \right] \quad (7)$$

with  $C_v = 1 / \sqrt{2\pi\Sigma_{s_v}}$ . Hereby, a pixel-wise independence of the image is assumed to simplify the computations.

Finally, the dynamic model input  $\mu'$  is also assumed to be noisy and follows a normal distribution with mean at the value of the function  $f(\mu, \rho) \in \mathbb{R}^4$  and with variance  $\Sigma_{s_\mu}$ :

$$p(\mu' | \mu) = C_\mu \prod_{i=1}^n \exp \left[ -\frac{1}{2\Sigma_{s_\mu}} (\mu'_i - f_i(\mu, \rho))^2 \right] \quad (8)$$

with  $C_\mu = 1 / \sqrt{2\pi\Sigma_{s_\mu}}$ .

The function  $f(\mu, \rho)$  is used to describe the system dynamics in our setting and depends on the current internal belief  $\mu$  and the causal variables  $\rho$ . In the reaching task this function is adapted to work as a perceptual attractor.

### D. Visual Forward Model: Convolutional Decoder

In order to perform pixel-based free-energy optimization, a visual forward model, which maps the internal belief (e.g. the body state or schema) to the expected visual sensation, is needed. This generative model is implemented as a convolutional decoder that outputs the predicted camera image given the robot's internal belief of its joint configurations.

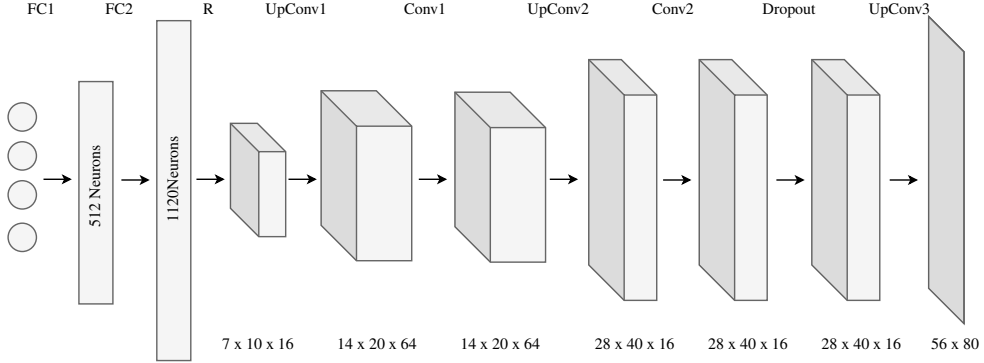


Fig. 2. Network Architecture of the Convolutional Decoder (FC: Fully-connected layer, R: Reshape operator, UpConv: Transposed Convolution, Conv: Convolution)

1) *Network Architecture*: The architecture of the convolutional decoder is depicted in figure 2. The network structure was based on the generative network proposed in [18].

The network input is the 4-dimensional internal belief of the body state  $\mu$ , which is in our case the four joint angles of the robot's left arm: shoulder roll, shoulder pitch, elbow yaw and elbow roll. The inputs go through 2 fully-connected layers (FC1 and FC2) and the resulting 1120-dimensional vector is reshaped into a  $7 \times 10 \times 16$  tensor. Afterwards, the transposed convolution (denoted by *UpConv* in fig. 2) is performed to upsample the image, which is an essential component of the network. The transposed convolution, also referred to as deconvolution, uses the input as the weights for the filters and can be regarded as a backward pass of the standard convolution operator. [19]. The UpConv layers all use stride equal to 2 and a padding of 1. Moreover, a kernel with size  $4 \times 4$  was chosen to avoid checkerboard artifacts due to uneven overlap [20]. Following the practice in [18], each transposed convolution layer was followed by a standard convolutional layer (kernel size 3, stride 1, padding 1), which helps to smooth out the potential artifacts from the transposed convolution step. There is an additional 1D-Dropout layer ( $p=0.15$ ) before the last transposed convolution layer to avoid overfitting and achieve better generalization performance. All layers use rectified linear unit (ReLU) as activation function, except for the last layer. In the final layer, a sigmoid function is used to get pixel intensity values in the range  $[0, 1]$ . Throughout the consecutive UpConv-Conv operations in the network, the number of channels is increased and decreased again to get an output image of size  $1 \times 56 \times 80$ . The output channel size is 1, since grayscale images were used in our framework to decrease the overall computational complexity for the free-energy optimization.

#### E. Pixel-Based Active Inference

Our goal is to update the internal belief and to generate actions by performing free-energy optimization using the terms  $\dot{\mu} = -\frac{\partial F}{\partial \mu}$  and  $\dot{a} = -\frac{\partial F}{\partial a}$ . The derivatives of the variational free energy  $F$  with respect to  $\mu$  and  $a$  are given as follows:

$$-\frac{\partial F}{\partial \mu} = \frac{1}{\Sigma_{s_v}} \left( \frac{\partial g(\mu)}{\partial \mu} \right)^T (s_v - g(\mu)) + \frac{1}{\Sigma_{s_\mu}} \left( \frac{\partial f(\mu, \rho)}{\partial \mu} \right)^T (\mu' - f(\mu, \rho)) \quad (9)$$

$$-\frac{\partial F}{\partial a} = -\frac{1}{\Sigma_{s_v}} \left( \frac{\partial s_v}{\partial a} \right)^T (s_v - g(\mu)) \quad (10)$$

Once these derivatives are computed, the free-energy can be minimized using a simple gradient descent approach:

$$\mu_{t+1} = \mu_t + \Delta_t \dot{\mu} \quad a_{t+1} = a_t + \Delta_t \dot{a} \quad (11)$$

1) **Backward Pass Through the Convolutional Decoder**: An essential term in the derivatives is  $\frac{\partial g(\mu)}{\partial \mu}$ . This term is computed by performing a backward pass over the convolutional decoder. It is important to note that since the function  $g(\cdot)$  outputs images of size  $w \times h$ ,  $\frac{\partial g(\mu)}{\partial \mu}$  is actually a three dimensional tensor. To simplify the notation, we will stack the output into a vector  $\in \mathbb{R}^{w \cdot h}$  (row major). The following equation is obtained:

$$-\frac{\partial F}{\partial \mu} = \underbrace{\begin{bmatrix} \frac{\partial g_{1,1}}{\partial \mu_1} & \frac{\partial g_{1,2}}{\partial \mu_1} & \cdots & \frac{\partial g_{w,h}}{\partial \mu_1} \\ \frac{\partial g_{1,1}}{\partial \mu_2} & \frac{\partial g_{1,2}}{\partial \mu_2} & \cdots & \frac{\partial g_{w,h}}{\partial \mu_2} \\ \vdots & \vdots & \vdots & \vdots \\ \frac{\partial g_{1,1}}{\partial \mu_4} & \frac{\partial g_{1,2}}{\partial \mu_4} & \cdots & \frac{\partial g_{w,h}}{\partial \mu_4} \end{bmatrix}}_{\left(\frac{\partial \mathbf{g}}{\partial \mu}\right)^T} \underbrace{\begin{bmatrix} \frac{\partial F}{\partial g_{1,1}} \\ \frac{\partial F}{\partial g_{1,2}} \\ \vdots \\ \frac{\partial F}{\partial g_{w,h}} \end{bmatrix}}_{\frac{\partial F}{\partial \mathbf{g}}}$$
(12)

where  $\frac{\partial F}{\partial g_{i,l}}$  is given by  $\frac{1}{\Sigma_{s_v}}(v_{i,l} - g(\mu_{i,l}))$ .

2) **Partial derivatives for the action:** The backward pass is also important for the computation of  $\frac{\partial s_v}{\partial a}$  in equation 10. The action values describe the velocities for the velocity controller at each timestep. The target values of the joint angles are then computed as:  $q_{t+1} = q_t + T a_t$ , where  $T$  is the duration of each iteration and has a fixed value. In a velocity controller scheme we can approximate that the angle change between two time steps is:

$$\frac{\partial q_i}{\partial a_j} = T \quad (13)$$

Then, assuming convergence for the sensation values at the equilibrium point with  $\mu \rightarrow s_p$  and  $\mathbf{g}(\mu) \rightarrow s_v$ , the term  $\frac{\partial s_v}{\partial a}$  can be computed using the following equation:

$$\frac{\partial s_v}{\partial a_j} = \frac{\partial s_v}{\partial q_j} \frac{\partial q_j}{\partial a_j} = \frac{\partial \mathbf{g}(\mu)}{\partial \mu_j} \frac{\partial \mu_j}{\partial a_j} \quad (14)$$

3) **Visual Attractor Dynamics:** The attractor dynamics is defined as follows:

$$\mathbf{f}(\mu, \rho) = \mathbf{T}(\mu) (\beta (\rho - \mathbf{g}(\mu))), \quad (15)$$

where  $\beta$  is a gain parameter and  $\mathbf{T}$  is the mapping from the pixel-domain to the joint space and is equal to  $\mathbf{T} = \left(\frac{\partial \mathbf{g}(\mu)}{\partial \mu}\right)^T$ . This term is computed by performing a backward pass through the convolutional decoder. Although the first-order dynamics are included since we use a velocity controller and want to include goal-directed behavior in the system,  $\mu'$  is not considered as part of the optimization problem itself. There are no updates performed on  $\mu'$  and it is set to zero in equation 9. This is done under the assumption that at equilibrium the robot's arm has converged to the attractor position, so that the mean of  $\mu'$ , given by  $\mathbf{f}(\mu, \rho)$ , goes to zero.

The term  $\frac{\partial \mathbf{f}(\mu, \rho)}{\partial \mu}$  in equation 9 is approximated by -1. This is done to avoid computing the Hessian in the convolutional decoder. These simplifications can be justified intuitively by inspecting equation 9. With these simplifications, we get:

$$-\frac{\partial F}{\partial \mu'} \frac{\partial \mu'}{\partial \mu} = \frac{1}{\Sigma_{s_\mu}} \left( \frac{\partial \mathbf{g}(\mu)}{\partial \mu} \right)^T [\beta(s_{attr} - \mathbf{g}(\mu))]$$

Although simplified considerably, this term is sufficient to generate an update for the internal belief  $\mu$  in the direction of the attractor image without increasing the computational cost of the algorithm significantly.

### III. EXPERIMENTAL SETUP

#### A. Simulated and real robot

The Aldebaran NAO humanoid robot was used for all the experiments. The simulator environment in Gazebo is depicted in figure 3(a). The torso was fixed in the world and the legs were removed from the simulator as they were not needed. The color of the right arm was changed to dark grey to achieve contrast with the grey background in the camera images.

Although the proprioceptive information is not be part of the free energy update scheme, the definition will also be given for the sake of completeness. The proprioceptive sensory information is provided by the joints encoder sensors  $s_p = [q_1, q_2, q_3, q_4]^T$ . It is assumed that the joint angle readings  $s_p$  are noisy and follow a normal distribution with mean at the internal belief value  $\mu$  and variance  $\Sigma_{s_p}$ , so that:

$$s_p \sim \mathcal{N}(\mu, \Sigma_{s_p}).$$

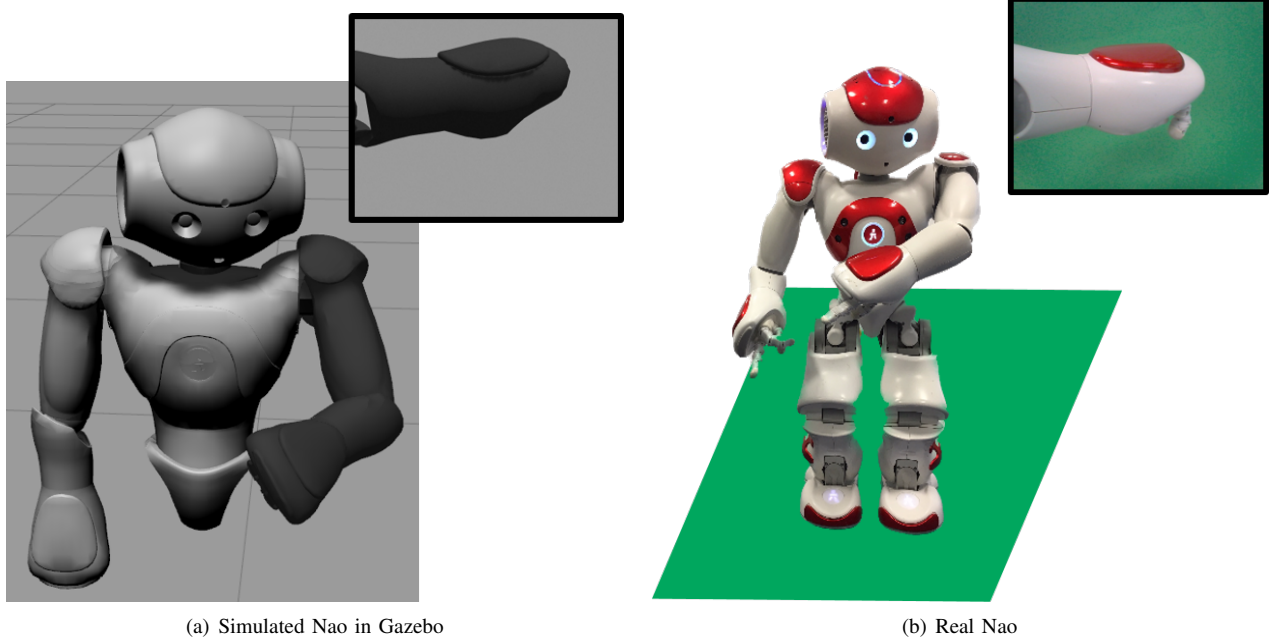


Fig. 3. Experimental setup in simulation and with the real robot.

### B. Visual Forward Model

*a) Data Acquisition & Preprocessing:* The dataset used to train the model consists of the left arm joint readings ( $s_p \in \mathbb{R}^4$ ) and the observed images obtained using NAO's bottom camera. The data samples were collected using three methods and these subsets were later concatenated to form the whole dataset.

First, the joint angles were drawn randomly from a uniform distribution in the range of the joint limits, but this approach required the manual elimination of samples where the robot's arm was out of the camera frame and the ratio of the acquired images with the robot hand centered in the camera image was significantly lower than the images with the hand located at the corners of the frame. To address this issue, in the second method, the robot's arm was manually moved by an operator and the joint angle readings were recorded during these trajectories. This way, a subset of data was obtained, where the robot hand was centered in the image. In the third method, a multivariate Gaussian was fit to the second subset using the expectation maximization algorithm and random samples were drawn from this Gaussian for the third and final part of the dataset. The goal was to introduce randomness to the centered-images and not be limited to the operator's choice of trajectories.

The final dataset consisted of 3200 data samples, where  $\sim 25\%$  was collected with method 1,  $\sim 20\%$  with method 2 and the remaining  $\sim 55\%$  using method 3.

For the images collected in the Gazebo NAO Simulator, the only preprocessing step performed was re-sizing the image of size  $640 \times 480$  to  $80 \times 56$ .

For the real NAO, the images were obtained on a green background (fig. 3(b)) and the following preprocessing steps were performed:

- 1) Median filtering with kernel size 11 on the original image.
- 2) Masking the green background in the HSV color space.
- 3) Applying a mono-chrome background (dark gray) and converting the image to grayscale
- 4) Resizing image to dimensions  $80 \times 56$ .

*b) Training:* The convolutional decoder was trained using the ADAM optimizer with an initial learning rate of  $\alpha = 10^{-4}$  with a mini-batch size of 200. The learning rate was decayed exponentially with the rate  $\gamma = 0.95$  every 5000 steps. The training was stopped after ca. 12000 iterations to avoid overfitting, as the test set error started to increase.

### C. Benchmark for PixelAI

A benchmark with 3 levels of difficulty was created to evaluate the performance of PixelAI on randomized samples for both perceptual and active inference. A set of 50 different cores (i.e. images of the arm) were generated by sampling the multivariate Gaussian distribution (see Method 2 in section III-B0a). A subset of the generated cores is shown in figure 5(a). For each of the 20 cores, 10 different random tests were performed. The 10 test samples for each core were generated differently depending on the benchmark level:

- Level 1 (close similar poses): One of the 4 joints was chosen randomly and a random perturbation  $\Delta \in \pm[5^\circ, 10^\circ]$  was sampled from a uniform distribution. This value was added to the core angle value to generate the perturbed new test sample.
- Level 2 (far similar poses): For all of the 4 joints, a random perturbation  $\Delta \in \mathbb{R}^4$  was sampled from a uniform distribution. These perturbations within the range  $\pm[5^\circ, 10^\circ]$  were added to the core joint angles.
- Level 3 (random): For each core, 10 different cores were chosen randomly and used as the test samples.

In total there were 5000 trials: 500 testing image arm poses per benchmark level, which were run 10 times.

a) **Perceptual Inference:** In order to evaluate the perceptual inference performance, the robot's arm was brought to the core positions. Then for each core, 10 separate test runs were performed, where the internal belief was set to a perturbed value of the corresponding core. These tests are static in nature, i.e. the change solely takes place in the internal predictions of the robot. The goal is that the robot internal belief  $\mu$  converges to the true arm position, which is equal to the joint angles of the chosen core.

b) **Active Inference:** In active inference, the core positions were treated as the imagined goal positions. These were the attractors in the model. Again for each core 10 separate test runs were performed, where the robot arm was moved to a perturbed value of the corresponding core and the initial internal belief was set to this value as well. This means that at timestep  $t = 0$ , we have:  $s_p = \mu$ .

In each test, the goal is that the robot internal belief  $\mu$  gets updated in the direction of the imaged arm position, the attractor. This change in the internal belief should then generate an action to compensate the mismatch between the current and the predicted visual sensations. In a successful test run, the robot arm should move to the imagined arm position and the internal belief should also converge to the imagined joint angles, so that:  $s_v = g(\mu) = s_{attr}$ .

#### D. Parameters for Active Inference

The parameters for active inference ( $\Sigma_{s_v}, \Sigma_{s_\mu}, \beta, \Delta_t$ ) were determined empirically. The intuition behind the variance terms is simple: The prediction errors get multiplied by the inverse of the variances so these actually weigh the relative influence of the corresponding sensory information error [21]. The  $\beta$  term, that is part of the attractor dynamics (see eq. 15) essentially has the same effect and it controls how much we want to push the internal belief in the direction of the attractor. Finally, the  $\Delta_t$  value can be thought of as the learning rate for the gradient descent optimization scheme. The parameters used for benchmark levels 1 and 2 were the same, only for level 3 a smaller initial parameter for  $\Sigma_{s_v}$  was used and after the visual prediction error was below a certain threshold (0.01), the same  $\Sigma_{s_v}$  value was used as for benchmark levels 1 and 2. This simple heuristic method of adaptation helped speed up the convergence for the more complex trajectories of level 3.

The generated actions (velocity values) were clipped so that each joint could not move more than  $[-2^\circ; 2^\circ]$  each time step. However, cases of action saturation were very rare and only happened in the level 3 tests.

## IV. RESULTS & DISCUSSION

### A. Perception in simulation

Perceptual inference tests were run for 5000 time steps for all 3 levels. An example of the perceptual inference for each level is depicted in Fig. IV-A. For level 1 and 2 with less than 150 iterations the algorithm converge to the ground truth, while inferring the body location from a totally random initialization rises considerably the complexity.

Table I shows the resulting average of the mean absolute error for each of the joints ( $|q_{true,i} - \mu_i|$ ). Level 1 and 2 results converged to internal belief values successfully. Figure 5 shows the error during the optimization process. Shoulder pitch and shoulder roll angles were estimated with better accuracy compared to the elbow angles. This is due to the fact that a small change in the shoulder pitch angle makes a greater difference in the visual field in comparison with the same amount of change in the elbow roll angle. Since *PixelAI* achieves perception by minimizing the visual prediction error, the accuracy increases when the pixel-based difference is stronger. Therefore, the mean error and standard deviation increase for the elbow joint angle estimations.

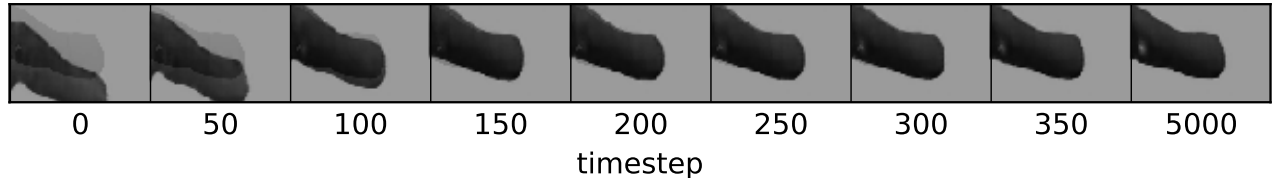
The errors in level 3, where the robot had to converge to random arm locations, were larger compared to levels 1 and 2, as shown in figure 6. This is due to two reasons. The first one is the local minima inherent of the gradient descent method. The second one affects the desired joint position, as depicted in Fig. 7. Several joint solutions produce small errors in the visual field strengthen the risk of getting stuck in a local minima.

### B. Perception and action in simulation

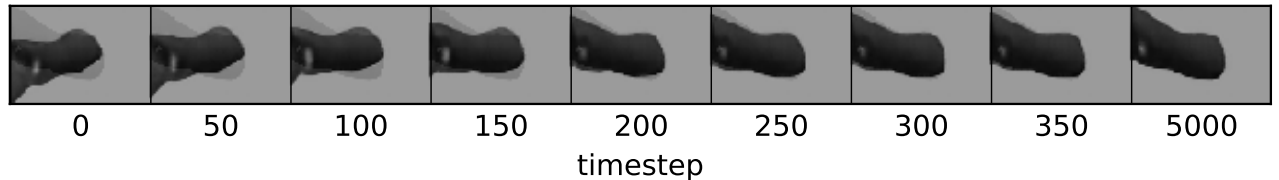
Active inference tests with goal images were performed first using the simulated NAO for 1000 iterations in levels 1, 2 and 3 of the benchmark. The results for levels 1 and 2 are depicted in figure 9. It can be seen here that the joint encoder readings follow the internal belief values through the actions generated by free-energy optimization. As expected, Level 3 results shows that interacting is more complex than perceiving as it includes the body and the world constraints. Larger values for  $\beta$  and smaller values for  $\Sigma_{s_v}$  were used to achieve faster convergence and amplify the actions.



(a) Level 1



(b) Level 2



(c) Level 3

Fig. 4. Example of the internal trajectories of the latent space during the perceptual inference tests for three different levels of difficulty for core 3.

Perceptual Inference: Joint Angles Mean Absolute Error (degrees)				
Level	Shoulder Pitch	Shoulder Roll	Elbow Yaw	Elbow Roll
1	0.265 ( $\pm 0.289$ )	0.342 ( $\pm 0.372$ )	0.762 ( $\pm 0.633$ )	1.190 ( $\pm 1.357$ )
2	0.358 ( $\pm 0.502$ )	0.487 ( $\pm 0.648$ )	0.884 ( $\pm 0.850$ )	1.661 ( $\pm 2.047$ )
3	5.028 ( $\pm 9.683$ )	6.370 ( $\pm 8.088$ )	15.763 ( $\pm 25.180$ )	14.667 ( $\pm 17.893$ )

TABLE I  
PREDICTION ERROR FOR PERCEPTUAL INFERENCE

### C. Active inference in the real robot

Perceptual Inference: Joint Angles Mean Absolute Error (degrees)				
Level	Shoulder Pitch	Shoulder Roll	Elbow Yaw	Elbow Roll
1	1.326 ( $\pm 0.823$ )	0.679 ( $\pm 0.773$ )	1.569 ( $\pm 1.441$ )	1.9690 ( $\pm 2.032$ )
2	1.862 ( $\pm 1.846$ )	2.221 ( $\pm 3.038$ )	2.935 ( $\pm 3.311$ )	3.807 ( $\pm 3.323$ )
3	9.799 ( $\pm 12.629$ )	12.773 ( $\pm 10.907$ )	29.354 ( $\pm 35.479$ )	21.818 ( $\pm 17.231$ )

TABLE II  
PREDICTION ERROR FOR PERCEPTUAL INFERENCE REAL ROBOT

The real robot add another extra level of difficulty since the robot's movements are imprecise due to the mechanical backlash in the actuators ( $\pm 5^\circ$ ) [22]. We converted the position control into a velocity control. Thus, the robot had to wait

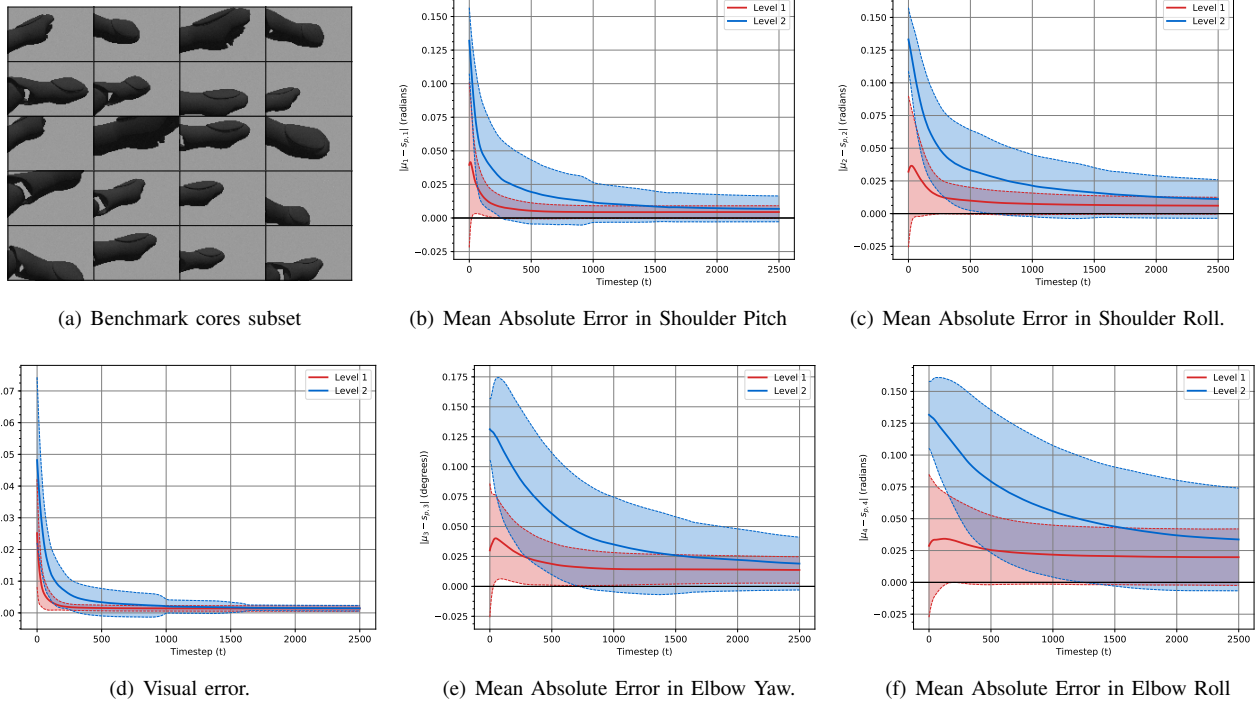


Fig. 5. Perceptual Inference Results: Results for level 1 (red) and level 2 (blue) of the benchmark are shown. Mean Absolute Error between internal state  $\mu_i$  and  $s_{p,i}$  for all 4 DOF of the left arm is plotted, as well as the visual prediction error 5(d)

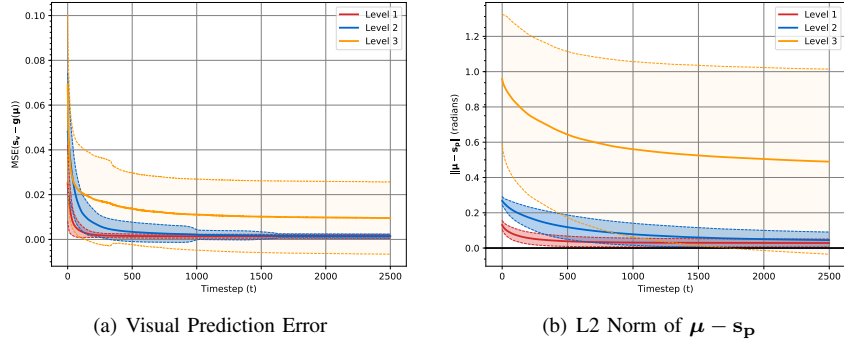


Fig. 6. Simulated NAO Perceptual Inference Results for all 3 Benchmark Levels

for the generated actions to be large enough, in order to send the commands to the controller. This caused the movements to be unsmooth. Moreover, as we did not have direct access to the motor driver, the time the action was executed had a large mismatch between the internal error and the actual arm position, resulting in a desynchronization in the internal model and real world, which can cause the system to diverge.

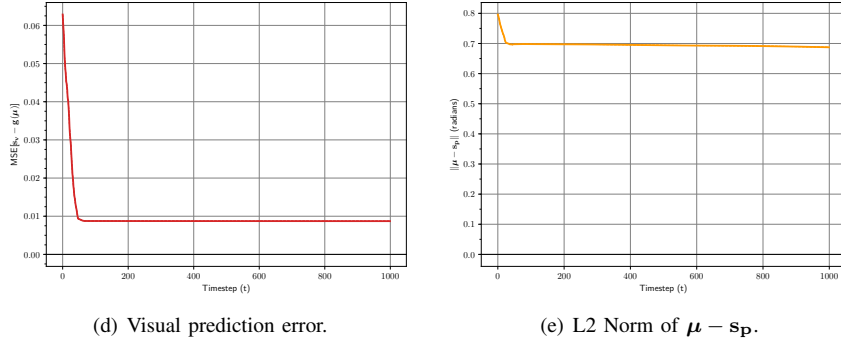
Furthermore, the visual forward model is expected to model the more complex structure of the real robot hand, that is subject to lighting differences and has a reflective surface. Unlike in the simulator, the same conditions cannot be restored perfectly in the real word, so the model training is always subject to additional noise in the dataset. We used the same deep convolutional decoder architecture for our tests on the real robot as well. Low training error was achieved on the training dataset (MSE in pixel-intensity: ca. 0.0015). The results of the perceptual inference for real NAO on all 3 benchmark levels are depicted in figure 8. Similar behaviours of perceptual convergence were found in Level 1 and 2, while level 3 had a larger error due to the local minima.

## V. VARIATIONAL FREE-ENERGY, AUTOENCODERS AND ACTIVE PERCEPTION

Both autoencoders and the free energy formulation [11] are sustained with the same variational learning theory [23] and solve the same problem. However, autoencoders are forgetting the original ideas from the Helmholtz machine [24]. Perception

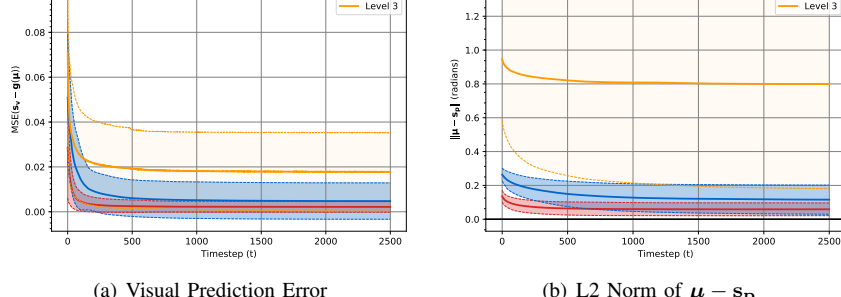


(a) True arm position (camera image). (b) Initial internal belief deep convolutional decoder output  $g(\mu)$  (overlaid on the camera image). (c) Deep convolutional decoder output  $g(\mu)$  for end internal belief (overlaid on the camera image).



(d) Visual prediction error. (e) L2 Norm of  $\mu - s_p$ .

Fig. 7. Example of the local minima problem in Level 3 perceptual inference tests.



(a) Visual Prediction Error (b) L2 Norm of  $\mu - s_p$

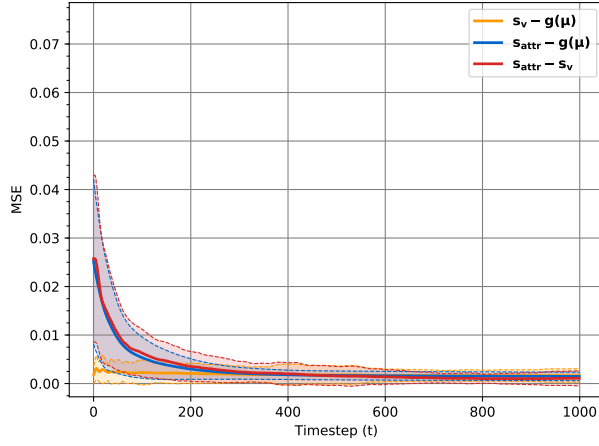
Fig. 8. Real NAO Perceptual Inference Results for all 3 Benchmark Levels

is an active continuous process [25]. Here we have shown how we can use variational inference to provide the active adaptation and interpolation to online input for perception and action. This allow us to incorporate priors (top-down modulation) and have inference dynamics without using recurrent neural networks. We can also exploit variational autoencoders to directly output the action. Furthermore, we can use variational free energy bound minimization as the general inner mechanism for both learning and adaptation to the environment.

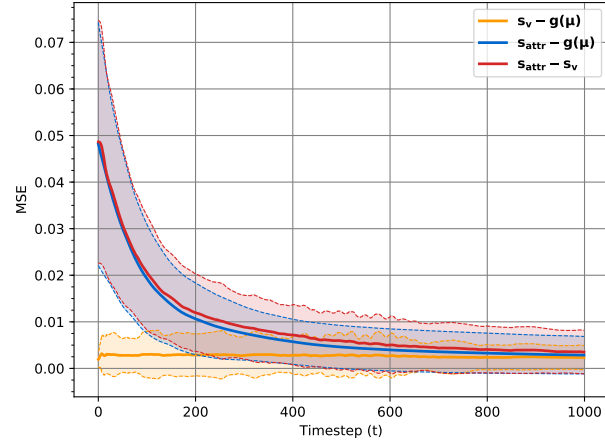
Regarding the action, we are solving the POMDP formulation without rewards, but we are coding the goal inside the attractor. How we can go from intention to the prior needed in active inference is not really clear and it is usually answered by the hierarchical structure. We can describe, for instance, a system that generates desired internal beliefs that are transformed into expected sensations that will drive the agent towards the goal, in line with the view of perception as a dynamical system [26]. Furthermore, our *pixelAI* algorithm complements the active inference community effort to provide scalable models for real applications [27], [28].

## VI. CONCLUSIONS

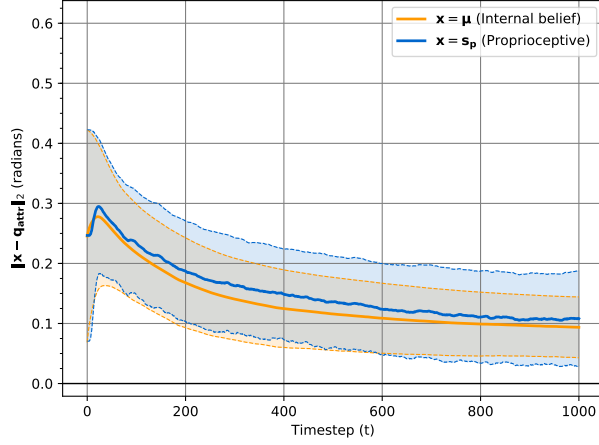
We have described a Pixel-based deep Active Inference algorithm and applied it for robot body perception and action. Our model-free algorithm enabled estimation of the robot arm joint states just using a monocular camera input and direct visual servoing using imaginary goals in the visual space. Statistical results showed convergence in both perception and action in



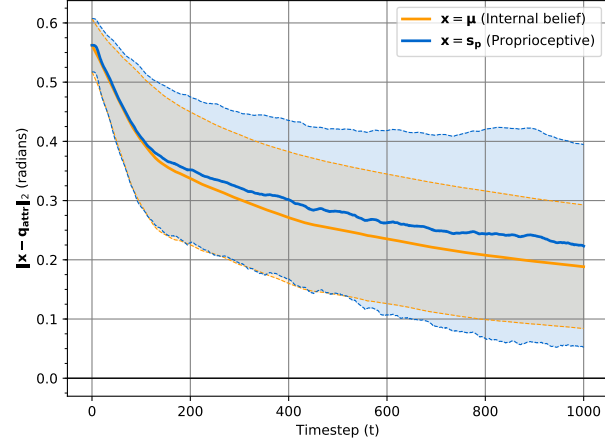
(a) Level 1: Visual error



(b) Level 2: Visual error

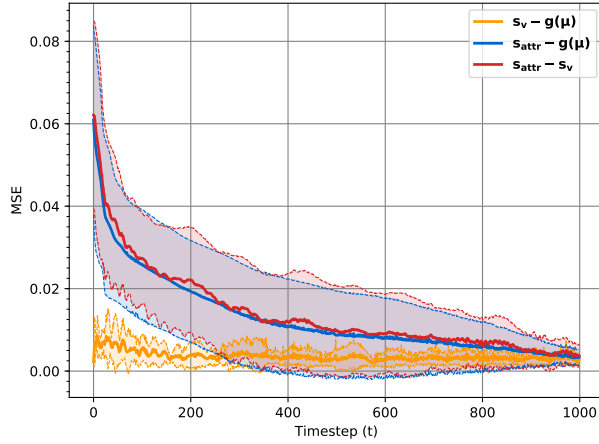


(c) Level 1: L2-Norm of Joint Angle Errors

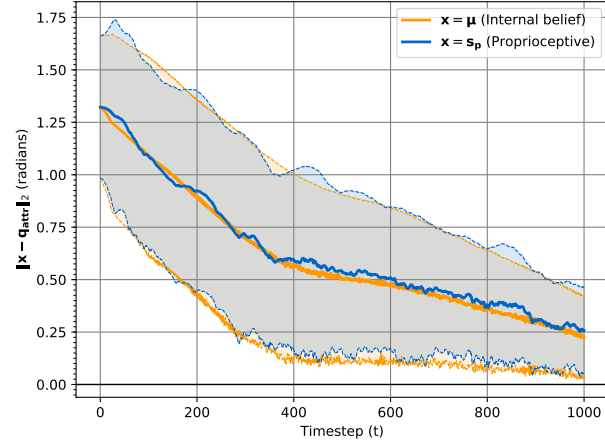


(d) Level 2: L2-Norm of Joint Angle Errors

Fig. 9. Simulated NAO active inference test results plotted separately for level 1 (left) and level 2 (middle) of the benchmark



(a) Level 3 Core 3: Visual error



(b) Level 3 Core 3: L2-Norm of Joint Angle Errors

Fig. 10. Simulated NAO active inference level 3 test results for one example core

different levels of difficulty with a larger error when inferring totally random arm poses. This neuroscience-inspired approach

allows us to make deeper interpretations than conventional engineering solutions [29], giving some grounding for novel machine learning developments, especially for body perception and action.

## REFERENCES

- [1] D. M. Wolpert, J. Diedrichsen, and J. R. Flanagan, "Principles of sensorimotor learning," *Nature Reviews Neuroscience*, vol. 12, no. 12, p. 739, 2011.
- [2] Y. Yamada, H. Kanazawa, S. Iwasaki, Y. Tsukahara, O. Iwata, S. Yamada, and Y. Kuniyoshi, "An embodied brain model of the human foetus," *Scientific Reports*, vol. 6, 2016.
- [3] M. Botvinick and J. Cohen, "Rubber hands feelouch that eyes see," *Nature*, vol. 391, no. 6669, p. 756, 1998.
- [4] N.-A. Hinz, P. Lanillos, H. Mueller, and G. Cheng, "Drifting perceptual patterns suggest prediction errors fusion rather than hypothesis selection: replicating the rubber-hand illusion on a robot," *arXiv preprint arXiv:1806.06809*, 2018.
- [5] K. Doya, "What are the computations of the cerebellum, the basal ganglia and the cerebral cortex?" *Neural networks*, vol. 12, no. 7-8, pp. 961–974, 1999.
- [6] S. Hutchinson, G. D. Hager, and P. I. Corke, "A tutorial on visual servo control," *IEEE transactions on robotics and automation*, vol. 12, no. 5, pp. 651–670, 1996.
- [7] C. G. Cifuentes, J. Issac, M. Wüthrich, S. Schaal, and J. Bohg, "Probabilistic articulated real-time tracking for robot manipulation," *IEEE Robotics and Automation Letters*, vol. 2, no. 2, pp. 577–584, 2016.
- [8] G. Oliver, P. Lanillos, and G. Cheng, "Active inference body perception and action for humanoid robots," *arXiv preprint arXiv:1906.03022*, 2019.
- [9] S. Levine, C. Finn, T. Darrell, and P. Abbeel, "End-to-end training of deep visuomotor policies," *The Journal of Machine Learning Research*, vol. 17, no. 1, pp. 1334–1373, 2016.
- [10] R. P. Rao and D. H. Ballard, "Predictive coding in the visual cortex: a functional interpretation of some extra-classical receptive-field effects," *Nature neuroscience*, vol. 2, no. 1, pp. 79–87, 1999.
- [11] K. J. Friston, "The free-energy principle: a unified brain theory?" *Nature Reviews Neuroscience*, vol. 11, pp. 127–138, 02 2010.
- [12] P. Lanillos, E. Dean-Leon, and G. Cheng, "Yielding self-perception in robots through sensorimotor contingencies," *IEEE Trans. on Cognitive and Developmental Systems*, no. 99, pp. 1–1, 2016.
- [13] G. Diez-Valencia, T. Ohashi, P. Lanillos, and G. Cheng, "Sensorimotor learning for artificial body perception," *arXiv preprint arXiv:1901.09792*, 2019.
- [14] K. Man and A. Damasio, "Homeostasis and soft robotics in the design of feeling machines," *Nature Machine Intelligence*, vol. 1, no. 10, pp. 446–452, 2019.
- [15] A. V. Nair, V. Pong, M. Dalal, S. Bahl, S. Lin, and S. Levine, "Visual reinforcement learning with imagined goals," in *Advances in Neural Information Processing Systems*, 2018, pp. 9191–9200.
- [16] G. E. Hinton and R. S. Zemel, "Autoencoders, minimum description length and helmholtz free energy," in *Advances in neural information processing systems*, 1994, pp. 3–10.
- [17] K. Friston, J. Mattout, N. Trujillo-Barreto, J. Ashburner, and W. Penny, "Variational free energy and the laplace approximation," *Neuroimage*, vol. 34, no. 1, pp. 220–234, 2007.
- [18] A. Dosovitskiy, J. T. Springenberg, M. Tatarchenko, and T. Brox, "Learning to generate chairs, tables and cars with convolutional networks," *IEEE transactions on pattern analysis and machine intelligence*, vol. 39, no. 4, pp. 692–705, 2016.
- [19] V. Dumoulin and F. Visin, "A guide to convolution arithmetic for deep learning," *arXiv preprint arXiv:1603.07285*, 2016.
- [20] A. Odena, V. Dumoulin, and C. Olah, "Deconvolution and checkerboard artifacts," *Distill*, vol. 1, no. 10, p. e3, 2016.
- [21] C. L. Buckley, C. S. Kim, S. McGregor, and A. K. Seth, "The free energy principle for action and perception: A mathematical review," *Journal of Mathematical Psychology*, 2017.
- [22] D. Gouaillier, C. Collette, and C. Kilner, "Omni-directional closed-loop walk for nao," in *2010 10th IEEE-RAS International Conference on Humanoid Robots*. IEEE, 2010, pp. 448–454.
- [23] D. P. Kingma and M. Welling, "Auto-encoding variational bayes," *arXiv preprint arXiv:1312.6114*, 2013.
- [24] P. Dayan, G. E. Hinton, R. M. Neal, and R. S. Zemel, "The helmholtz machine," *Neural computation*, vol. 7, no. 5, pp. 889–904, 1995.
- [25] R. Bajcsy, Y. Aloimonos, and J. K. Tsotsos, "Revisiting active perception," *Autonomous Robots*, vol. 42, no. 2, pp. 177–196, 2018.
- [26] J. Tani, *Exploring robotic minds: actions, symbols, and consciousness as self-organizing dynamic phenomena*. Oxford University Press, 2016.
- [27] A. Tschantz, M. Baltieri, A. Seth, C. L. Buckley *et al.*, "Scaling active inference," *arXiv preprint arXiv:1911.10601*, 2019.
- [28] B. Millidge, "Deep active inference as variational policy gradients," *arXiv preprint arXiv:1907.03876*, 2019.
- [29] D. Hassabis, D. Kumaran, C. Summerfield, and M. Botvinick, "Neuroscience-inspired artificial intelligence," *Neuron*, vol. 95, no. 2, pp. 245–258, 2017.